

iNeRF: Inverting Neural Radiance Fields for Pose Estimation

Lin Yen-Chen^{1,2}

Alberto Rodriguez²

¹Google Research

Pete Florence¹

Phillip Isola²

²Massachusetts Institute of Technology

Jonathan T. Barron¹

Tsung-Yi Lin¹

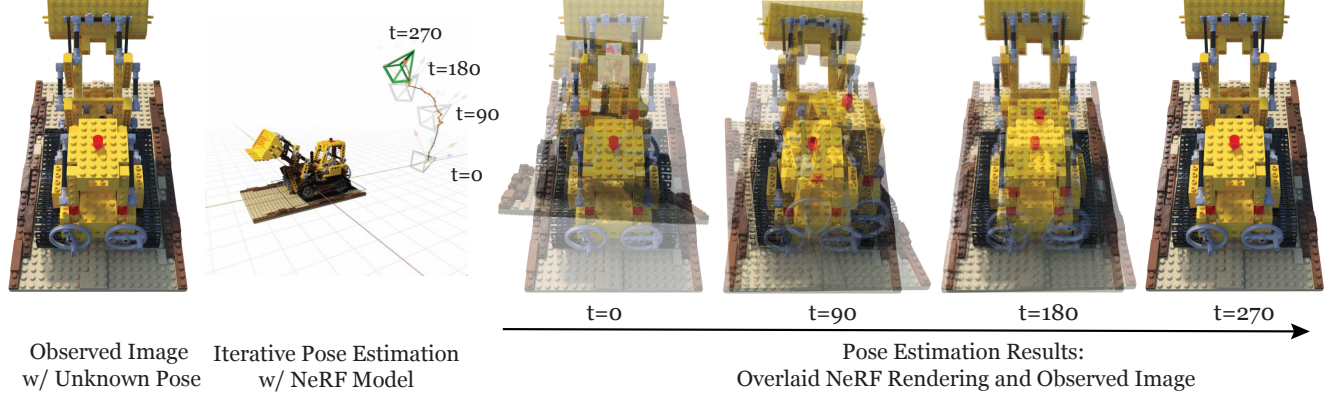


Figure 1: We present iNeRF which performs pose estimation by inverting an optimized neural radiance field representation of a scene. The middle figure shows the trajectory of estimated poses (gray) and the ground truth pose (green) in iNeRF’s iterative pose estimation procedure. By comparing the observed and rendered images, we perform gradient-based optimization to estimate the camera pose associated with the observed image. [Click the image to play the video in a browser](#).

Abstract

We present *iNeRF*, a framework that performs pose estimation by “inverting” a trained Neural Radiance Field (NeRF). NeRFs have been shown to be remarkably effective for the task of view synthesis — synthesizing photorealistic novel views of real-world scenes or objects. In this work, we investigate whether we can apply analysis-by-synthesis with NeRF for 6DoF pose estimation — given an image, find the translation and rotation of a camera relative to a 3D model. Starting from an initial pose estimate, we use gradient descent to minimize the residual between pixels rendered from an already-trained NeRF and pixels in an observed image. In our experiments, we first study 1) how to sample rays during pose refinement for *iNeRF* to collect informative gradients and 2) how different batch sizes of rays affect *iNeRF* on a synthetic dataset. We then show that for complex real-world scenes from the LLFF dataset, *iNeRF* can improve NeRF by estimating the camera poses of novel images and using these images as additional training data for NeRF. Finally, we show *iNeRF* can be combined with feature-based pose initialization. The approach outperforms all other RGB-based methods relying on synthetic data on LineMOD.

1. Introduction

Neural Radiance Fields (NeRF) have exhibited an exceptional ability to recover the 3D geometry and appearance of a scene for the purpose of novel view synthesis. NeRF learns a neural representation of a scene by training on multiple images with given camera poses, in which the density and color of the scene are parameterized as a function of 3D scene coordinates. Here we present iNeRF, a new framework for 6 DoF pose estimation by inverting a NeRF model. iNeRF takes three inputs: an observed image, an initial estimate of the pose, and a trained NeRF model representing a 3D scene or an object in the image. We adopt an analysis-by-synthesis approach to compute the appearance differences between the pixels rendered from the trained NeRF model and the pixels from the observed image. The gradients from these residuals are then backpropagated through the NeRF model to produce the gradients for the estimated pose. This procedure is repeated iteratively until the rendered and observed images are aligned, thereby yielding an accurate pose estimate.

6 DoF pose estimation has a wide range of applications, including augmented reality and robot manipulation [21, 22]. Recent progress in differentiable rendering has sparked interest in solving pose estimation via analysis-by-

synthesis [4, 19, 31, 48]. However, techniques built around differentiable rendering engines typically require a high-quality watertight 3D model of the object for use in rendering. Obtaining such models can be difficult and labor-intensive, and objects with unusual transparencies, shapes, or material properties may not be amenable to the 3D model format used by the rendering engine. NeRF provides a mechanism for capturing complex 3D and optical structure from only a set of RGB images, which opens up the opportunity to apply analysis-by-synthesis to broader real-world scenarios.

Despite its compelling reconstruction ability, using NeRF as a differentiable renderer for pose estimation through gradient-based optimization presents several challenges. For one, NeRF renders each pixel in an image by shooting a ray through that pixel and repeatedly querying a 3D radiance field (parameterized by a neural network) while marching along that ray to produce estimates of volume density and color that are then alpha-composited into a pixel color. This rendering procedure is expensive, which presents a problem for an analysis-by-synthesis approach which, naively, should require rendering a complete image and backpropagating the loss contributed by all pixels. For iNeRF, we address this issue by capitalizing on the fact that NeRF’s ray-marching structure allows rays and pixels to be rendered individually, and we present an interest point-based sampling approach that allows us to identify *which rays* should be sampled to best inform the pose of the object. This sampling strategy allows for accurate pose estimation while using two orders of magnitude fewer pixels than a full-image sampling.

Furthermore, we study the setting when only a subset of the observed images have corresponding poses, which happens when observations are captured with devices that have multiple calibrated cameras such as cell phones or self-driving cars. We demonstrate iNeRF can improve NeRF’s reconstruction quality by annotating images without pose labels and adding them to the training set. We show that this procedure can reduce the number of required labeled images by 25% while maintaining reconstruction quality.

To summarize, we explore the application of 6 DoF pose estimation by inverting a trained NeRF model, where our primary contributions are as follows:

- We show that iNeRF can use a trained NeRF model to estimate 6 DoF pose for scenes and objects with complex geometry, without the use of 3D CAD models or depth sensing — only RGB images are used as input.
- We show that iNeRF can improve NeRF by predicting the camera poses of additional images, that can then be added into NeRF’s training set.
- We perform a thorough investigation of ray sampling and the batch sizes for gradient optimization to characterize the robustness and limitations of iNeRF.

2. Related Works

Neural 3D shape representations. Recently, several works have investigated representing 3D shapes implicitly with neural networks. In this formulation, the geometric or appearance properties of a 3D point $\mathbf{x} = (x, y, z)$ is parameterized as the output of a neural network. The advantage of this approach is that scenes with complex topologies can be represented at high resolution with low memory usage. When ground truth 3D geometry is available as supervision, neural networks can be optimized to represent the signed distance function [30] or occupancy function [25]. However, ground truth 3D shapes are hard to obtain in practice. This motivates subsequent work on relaxing this constraint by formulating differentiable rendering pipelines that allow neural 3D shape representations to be learned using only 2D images as supervision [12, 15, 16]. Niemeyer *et al.* [28] represent a surface as a neural 3D occupancy field and texture as a neural 3D texture field. Ray intersection locations are first computed with numerical methods using the occupancy field and then provided as inputs to the texture field to output the colors. Scene Representation Networks [38] learn a neural 3D representation that outputs a feature vector and RGB color at each continuous 3D coordinate and employs a recurrent neural network to perform differentiable ray-marching. NeRF [27] shows that by taking view directions as additional inputs, a learned neural network works well in tandem with volume rendering techniques and enables photo-realistic view synthesis. NeRF in the Wild [23] extends NeRF to additionally model each image’s individual appearance and transient content, thereby allowing high-quality 3D reconstruction of landmarks using unconstrained photo collections. NSVF [17] improves NeRF by incorporating a sparse voxel octree structure into the scene representation, which accelerates rendering by allowing voxels without scene content to be omitted during rendering. Unlike NeRF and its variants, which learn to represent a scene’s structure from posed RGB images, we address the inverse problem: how to localize new observations whose camera poses are unknown, using an already-trained NeRF.

Pose Estimation from RGB Images. Classical methods for object pose estimation address the task by detecting and matching keypoints with known 3D models [1, 5, 7, 33]. Recent approaches based on deep learning have proposed to 1) directly estimate objects pose using CNN-based architectures [36, 44, 50] or 2) estimate 2D keypoints [32, 40, 42, 43] and solve for pose using the PnP-RANSAC algorithm. Differentiable mesh renderers [3, 29] have also been explored for pose estimation. Although their results are impressive, all the aforementioned works require access to objects’ 3D models during both training and test-

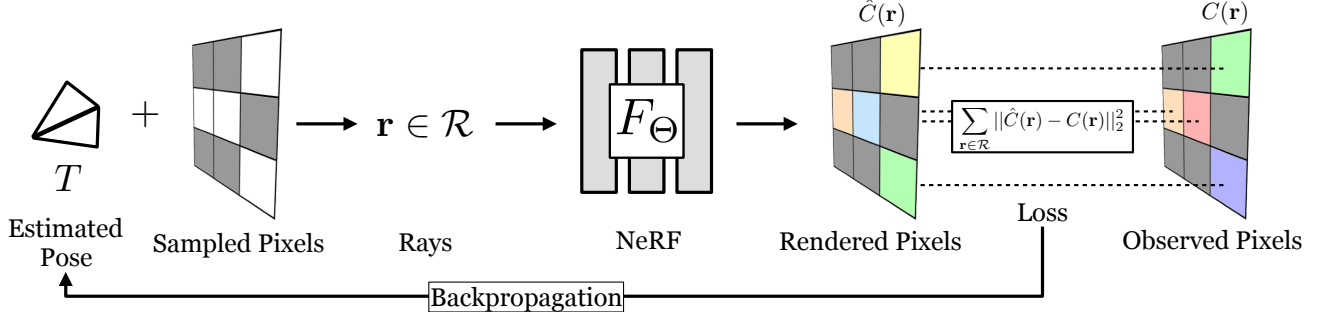


Figure 2: An overview of our pose estimation pipeline which inverts an optimized neural radiance field (NeRF). Given an initially estimated pose, we first decide which rays to emit. Sampled points along the ray and the corresponding viewing direction are fed into NeRF’s volume rendering procedure to output rendered pixels. Since the whole pipeline is differentiable, we can refine our estimated pose by minimizing the residual between the rendered and observed pixels.

ing, which significantly limits the applicability of these approaches. Recently, Chen *et al.* [4] address categorical object pose estimation [49] by performing single-view reconstruction with a 3D feature volume and then estimating pose using iterative image alignment. Because it is limited by the size of its 3D feature volume, this method cannot generate photo-realistic view synthesis or reconstruct unbounded scenes. To address these limitations, we investigate how to estimate poses when objects or scenes are represented as NeRFs. While *object pose estimation* methods are often separate from methods used for *visual localization* of a camera in a scene as in the SfM literature (i.e. [37, 45, 35]), because NeRF and iNeRF only require posed RGB images as training, iNeRF can be applied to localization as well.

3. Background

Given a collection of N RGB images $\{I_i\}_{i=1}^N$, $I_i \in [0, 1]^{H \times W \times 3}$ with known camera poses $\{T_i\}_{i=1}^N$, NeRF learns to synthesize novel views associated with unseen camera poses. NeRF does this by representing a scene as a “radiance field”: a volumetric density that models the shape of the scene, and a view-dependent color that models the appearance of occupied regions of the scene, both of which lie within a bounded 3D volume. The density σ and RGB color c of each point are parameterized by the weights Θ of a multilayer perceptron (MLP) F that takes as input the 3D position of that point $\mathbf{x} = (x, y, z)$ and the unit-norm viewing direction of that point $\mathbf{d} = (d_x, d_y, d_z)$, where $(\sigma, c) \leftarrow F_\Theta(\mathbf{x}, \mathbf{d})$. To render a pixel, NeRF emits a camera ray from the center of the projection of a camera through that pixel on the image plane. Along the ray, a set of points are sampled for use as input to the MLP which outputs a set of densities and colors. These values are then used to approximate the image formation behind volume rendering [11] using numerical quadrature [24], producing an estimate of the color of that pixel. NeRF is trained to

minimize a photometric loss $\mathcal{L} = \sum_{\mathbf{r} \in \mathcal{R}} \|\hat{C}(\mathbf{r}) - C(\mathbf{r})\|_2^2$, using some sampled set of rays $\mathbf{r} \in \mathcal{R}$ where $C(\mathbf{r})$ is the observed RGB value of the pixel corresponding to ray \mathbf{r} in some image, and $\hat{C}(\mathbf{r})$ is the prediction produced from neural volume rendering. To improve rendering efficiency one may train two MLPs: one “coarse” and one “fine”, where the coarse model serves to bias the samples that are used for the fine model. Though NeRF and its variants have been successful in producing photorealistic renderings, they are known to be slow because rendering a pixel requires multiple evaluations of a neural network at all the sampled points along a ray, which is expensive. For more details, we refer readers to Mildenhall *et al.* [27].

4. iNerf Formulation

We now present iNeRF, a framework that performs 6 DoF pose estimation by “inverting” a trained NeRF. Let us assume that the NeRF of a scene or object parameterized by Θ has already been recovered and that the camera intrinsics are known, but the camera pose T of an image observation I are as-yet undetermined. Unlike NeRF, which optimizes Θ using a set of given camera poses and image observations, we instead solve the inverse problem of recovering the camera pose T given the weights Θ and the image I as input:

$$\hat{T} = \underset{T \in \text{SE}(3)}{\operatorname{argmin}} \mathcal{L}(T | I, \Theta) \quad (1)$$

To solve this optimization, we use the ability from NeRF to take some estimated camera pose $T \in \text{SE}(3)$ in the coordinate frame of the NeRF model and render a corresponding image observation. We can then use the same photometric loss function \mathcal{L} as was used in NeRF (Sec. 3), but rather than backpropagate to update the weights Θ of the MLP, we instead update the pose T to minimize \mathcal{L} . While the concept of inverting a NeRF to perform pose estimation can be concisely stated, it is not obvious that such a problem

can be practically solved to a useful degree. The loss function \mathcal{L} is non-convex over the 6DoF space of $\text{SE}(3)$, and full-image NeRF renderings are computationally expensive, particularly if used in the loop of an optimization procedure. Our formulation and experimentation (Sec. 5) aim to address these challenges. In the next sections, we discuss (i) the gradient-based $\text{SE}(3)$ optimization procedure, (ii) ray sampling strategies, and (iii) how to use iNeRF’s predicted poses to improve NeRF.

4.1. Gradient-Based $\text{SE}(3)$ Optimization

Let Θ be the parameters of a trained and fixed NeRF, \hat{T}_i the estimated camera pose at current optimization step i , I the observed image, and $\mathcal{L}(\hat{T}_i | I, \Theta)$ be the loss used to train the fine model in NeRF. We employ gradient-based optimization to solve for \hat{T} as defined in Equation 1. To ensure that the estimated pose \hat{T}_i continues to lie on the $\text{SE}(3)$ manifold during gradient-based optimization, we parameterize \hat{T}_i with exponential coordinates. Given an initial pose estimate $\hat{T}_0 \in \text{SE}(3)$ from the camera frame to the model frame, we represent \hat{T}_i as:

$$\hat{T}_i = e^{[\mathcal{S}_i]\theta_i} \hat{T}_0,$$

where $e^{[\mathcal{S}]\theta} = \begin{bmatrix} e^{[\omega]\theta} & K(\mathcal{S}, \theta) \\ 0 & 1 \end{bmatrix}$,

where $\mathcal{S} = [\omega, \nu]^T$ represents the screw axis, θ the magnitude, $[\omega]$ represents the skew-symmetric 3×3 matrix of w , and $K(\mathcal{S}, \theta) = (I\theta + (1 - \cos \theta)[\omega] + (\theta - \sin \theta)[\omega]^2)\nu$ [18]. With this parameterization, our goal is to solve the optimal relative transformation from an initial estimated pose T_0 :

$$\widehat{\mathcal{S}\theta} = \underset{\mathcal{S}\theta \in \mathbb{R}^6}{\operatorname{argmin}} \mathcal{L}(e^{[\mathcal{S}]\theta} T_0 | I, \Theta). \quad (2)$$

We iteratively differentiate the loss function through the MLP to obtain the gradient $\nabla_{\mathcal{S}\theta} \mathcal{L}(e^{[\mathcal{S}]\theta} T_0 | I, \Theta)$ that is used to update the estimated relative transformation. We use Adam optimizer [13] with an exponentially decaying learning rate (See Supplementary for parameters). For each observed image, we initialize $\mathcal{S}\theta$ near 0, where each element is drawn at random from a zero-mean normal distribution $\mathcal{N}(0, \sigma = 10^{-6})$. In practice, parameterizing with $e^{[\mathcal{S}]\theta} T_0$ rather than $T_0 e^{[\mathcal{S}]\theta}$ results in a center-of-rotation at the initial estimate’s center, rather than at the camera frame’s center. This alleviates coupling between rotations and translations during optimization.

4.2. Sampling Rays

In a typical differentiable render-and-compare pipeline, one would want to leverage the gradients contributed by all of the output pixels in the rendered image [48]. However, with NeRF, each output pixel’s value is computed by weighing the values of n sampled points along each ray $\mathbf{r} \in \mathcal{R}$

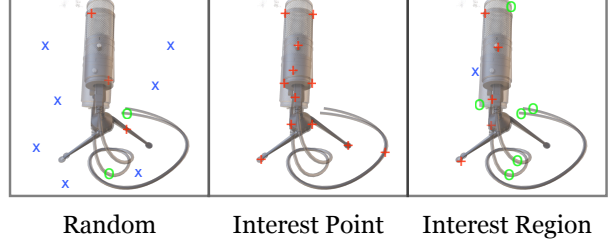


Figure 3: An illustration of 3 sampling strategies. The input image and the rendering corresponding to the estimated pose of the scene are averaged. We use x to represent sampled pixels on the background; $+$ to represent sampled pixels that are covered by both rendered and observed images; o to represent sampled pixels that are only covered by either the rendered or the input image. When performing random sampling (left) many sampled pixels are x , which provide no gradients for updating the pose. For “interest point” sampling (middle) some of the sampled pixels are already aligned and therefore provide little information. For “interest region” sampling, many sampled pixels are o , which helps pose estimation achieve higher accuracy and faster convergence.

during ray marching, so given the amount of sampled rays in a batch $b = |\mathcal{R}|$, then $\mathcal{O}(bn)$ forward/backward passes of the underlying NeRF MLP will be queried. Computing and backpropagating the loss of all pixels in an image (*i.e.*, $b = HW$, where H and W represent the height and width of a high-resolution image) therefore require significantly more memory than is present on any commercial GPU. While we may perform multiple forward and backward passes to accumulate these gradients, this becomes prohibitively slow to perform each step of our already-iterative optimization procedure. In the following, we explore strategies for selecting a sampled set of rays \mathcal{R} for use in evaluating the loss function \mathcal{L} at each optimization step. In our experiments we find that we are able to recover accurate poses while sampling only $b = 2048$ rays per gradient step, which corresponds to a single forward/backward pass that fits within GPU memory and provides $150\times$ faster gradient steps on a 640×480 image.

Random Sampling. An intuitive strategy is to sample M pixel locations $\{p_x^i, p_y^i\}_{i=0}^M$ on the image plane randomly and compute their corresponding rays. Indeed, NeRF itself uses this strategy when optimizing Θ (assuming image batching is not used). We found this random sampling strategy’s performance to be ineffective when the batch size of rays b is small. Most randomly-sampled pixels correspond to flat, textureless regions of the image, which provide little information with regards to pose (which is consistent with the well-known aperture problem [46]). See Figure 3 for an illustration.

Interest Point Sampling. Inspired by the literature of image alignment [41], we propose interest point sampling to guide iNeRF optimization, where we first employ interest point detectors to localize a set of candidate pixel locations in the observed image. We then sample M points from the detected interest points and fall back to random sampling if not enough interest points are detected. Although this strategy makes optimization converge faster since less stochasticity is introduced, we found that it is prone to local minima as it only considers interest points on the observed image instead of interest points from both the observed and rendered images. However, obtaining the interest points in the rendered image requires $\mathcal{O}(HWn)$ forward MLP passes and thus prohibitively expensive to be used in the optimization.

Interest Region Sampling. To prevent the local minima caused by only sampling from interest points, we propose using “Interest Region” Sampling, a strategy that relaxes Interest Point Sampling and samples from the dilated masks centered on the interest points. After the interest point detector localizes the interest points, we apply a 5×5 morphological dilation for I iterations to enlarge the sampled region. In practice, we find this to speed up the optimization when the batch size of rays is small. Note that if I is set to a large number, Interest Region Sampling falls back to Random Sampling.

4.3. Self-Supervising NeRF with iNeRF

In addition to using iNeRF to perform pose estimation given a trained NeRF, we also explore using the estimated poses to feed back into training the NeRF representation. Specifically, we first (1) train a NeRF given a set of training RGB images with known camera poses $\{(I_i, T_i)\}_{i=1}^{N_{\text{train}}}$, yielding NeRF parameters Θ_{train} . We then (2) use iNeRF to take in additional unknown-pose observed images $\{I_i\}_{i=1}^{N_{\text{test}}}$ and solve for estimated poses $\{\hat{T}_i\}_{i=1}^{N_{\text{test}}}$. Given these estimated poses, we can then (3) use the self-supervised pose labels to add $\{(I_i, \hat{T}_i)\}_{i=1}^{N_{\text{test}}}$ into the training set. This procedure allows NeRF to be trained in a semi-supervised setting.

5. Results

We first conduct extensive experiments on the synthetic dataset from NeRF [27] and the real-world complex scenes from LLFF [26] to evaluate iNeRF for 6DoF pose estimation. Specifically, we study how the batch size of rays and sampling strategy affects iNeRF. We then show that iNeRF can improve NeRF by estimating the camera poses of images with unknown poses and using these images as additional training data for NeRF. Finally, we show that iNeRF works well in tandem with a feature-based object pose estimation pipeline, achieving competitive results against other pose estimation methods on real-world LineMOD

data when only synthetic training data is used.

5.1. Synthetic Dataset

We test iNeRF on 8 scenes from NeRF’s synthetic dataset. For each scene, we choose 5 test images and generate 5 different pose initializations by first randomly sampling an axis from the unit sphere and rotating the camera pose around the axis by a random amount within $[-40, 40]$ degrees. Then, we translate the camera along each axis by a random offset within $[-0.2, 0.2]$ meters.

Results. We report the percentage of predicted poses whose error is less than 5° or 5cm at different numbers of steps. Quantitative results are shown in Figure 6a. We verify that under the same sampling strategy, larger batch sizes of rays achieve not only better pose estimation accuracy, but also faster convergence. On the other hand, when the batch size of rays is fixed, interest region sampling is able to provide better accuracy and efficiency. Specifically, the qualitative results shown in Figure 4 clearly indicate that random sampling is inefficient as many sampled points lie on the common background and therefore provide no gradient for matching.

5.2. LLFF Dataset

We use 4 complex scenes: *Fern*, *Fortress*, *Horns*, and *Room* from the LLFF dataset [26]. For each test image, we generate 5 different pose initializations following the procedures outlined in Section 5.1 but instead translate the camera along each axis by a random offset within $[-0.1, 0.1]$ meters. Unlike the synthetic dataset where the images are captured on a surrounding hemisphere, images in the LLFF dataset are all captured with a forward-facing handheld cell-phone.

Pose Estimation Results. The percentage of predicted poses whose error is less than 5° or 5cm at different number of steps is reported in Figure 6b. Similar to Section 5.1, we find that the batch size of rays significantly affects iNeRF’s visual localization performance. Also, we notice that iNeRF performs worse on the LLFF dataset compared to the synthetic dataset. When the batch size of rays is set to 1024, the percentage of $< 5^\circ$ rotation errors drops from 71% to 55%, and the percentage of $< 5\text{cm}$ translation errors drops from 73% to 39%. This difference across datasets may be due to the fact that the LLFF use-case in NeRF uses a normalized device coordinate (NDC) space, or may simply be a byproduct of the difference in scene content.

Self-Supervising NeRF with iNeRF Results. We take the *Fern* scene from the LLFF dataset and train it with 25%, 50%, and 100% of the training data, respectively. Then,

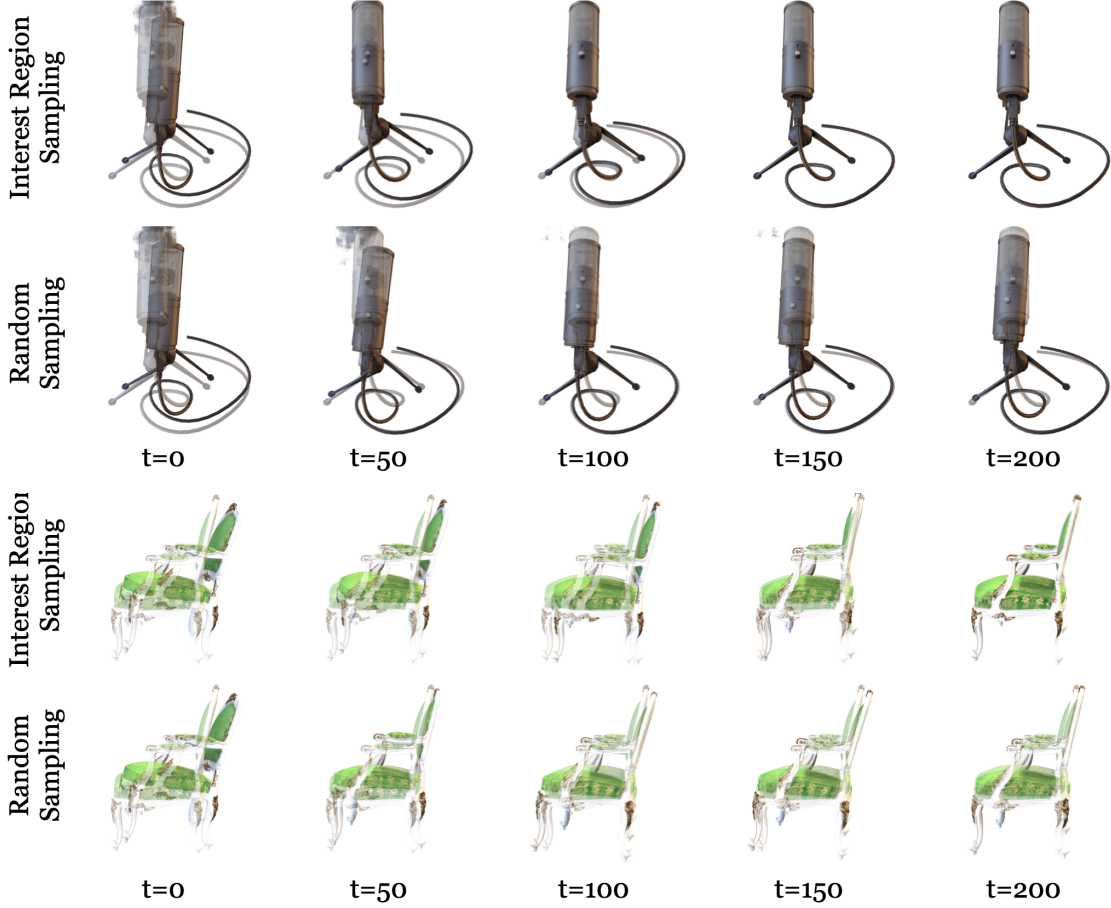


Figure 4: A comparison of pose estimation using test-set views of scenes from NeRF’s synthetic dataset. Rendered images based on the estimated pose at time t and the test image are visualized by averaging them. Our method is able to recover the camera pose by aligning the images. Adopting Interest Region Sampling helps our method to recover camera poses that align the rendered and test image to fine details. Random Sampling results in the Mic’s rigging being aligned, but fails to align the wire, and it also fails to align the Chair’s back. [Click the image to play the video in a browser.](#)

NeRFs trained with 25% and 50% data are used by iNeRF to estimate the remaining training images’ camera poses. The estimated camera poses, together with existing camera poses, are used as supervision to re-train NeRF from scratch. We report PSNRs in Table 1. All of the models are trained for 200k iterations using the same learning rate. We find that models that use the additional data made available through the use of iNeRF’s estimated poses perform better. This finding is consistent with NeRF’s well-understood sensitivity to the pose of its input cameras being accurate [27]. Qualitative results can be found in Figure 5.

5.3. LineMOD Dataset

To evaluate iNeRF for object pose estimation, we benchmark on the commonly used LineMOD dataset [9]. LineMOD provides synthetic training and real test data.

Label Fraction	100%		50%		25%	
iNeRF Supervision	No	Yes	No	Yes	No	
PSNR	24.94	24.64	24.18	23.89	21.85	

Table 1: Benchmark on *Fern* scene. NeRFs trained with pose labels generated by iNeRF can achieve higher PSNR.

The domain gap between the training and test data includes lighting, texture, and imperfect reconstruction [48]. Unlike methods [14, 51] which additionally train on 15% of the test data and thus have access to the real images and pose labels to close the domain gap, we train NeRFs only using the synthetic posed images following [10]. For a fair comparison, we follow previous works [48] to distinguish between training with and without pose labels of the real images sampled from the original test data. All the methods are evaluated on the remaining 85% of the test data.

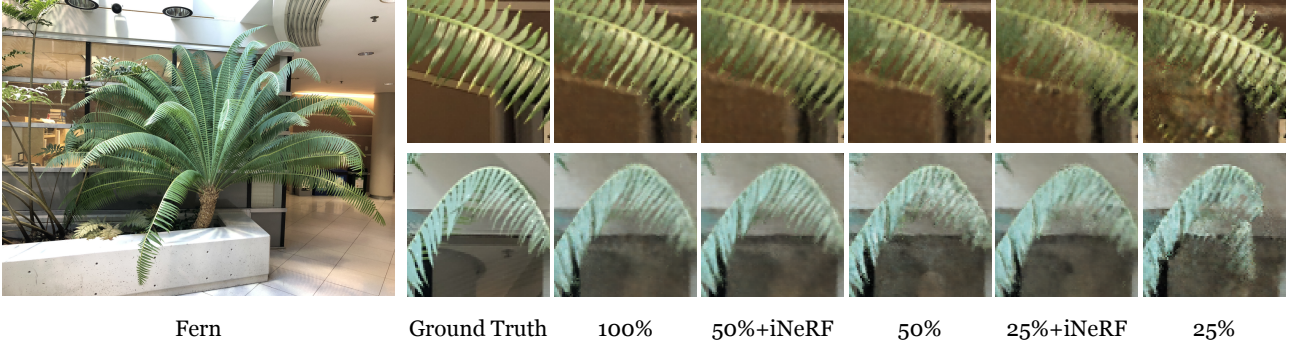


Figure 5: iNeRF can be used to improve NeRF by augmenting training data with images whose camera poses are unknown. We present an ablation study using 25% and 50% of training images to train NeRF models. These models are compared with models trained using 100% of the training images but where a fraction of that data use estimated poses from iNeRF rather than ground-truth poses from the dataset.

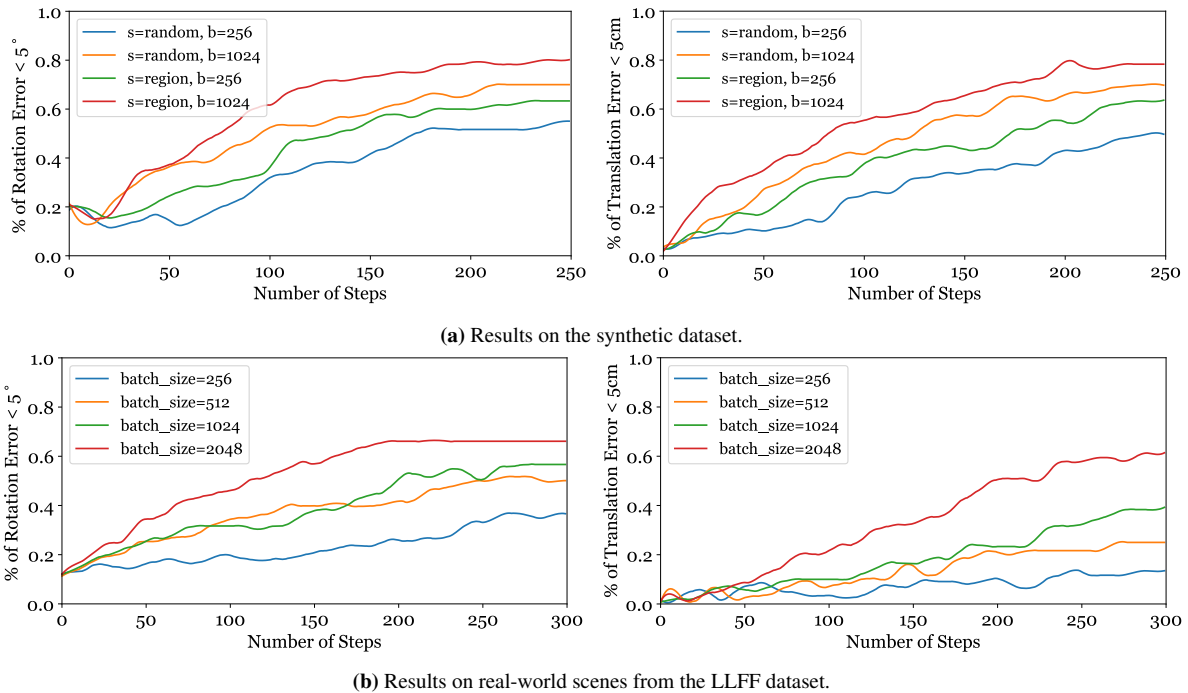


Figure 6: Quantitative results. “s” stands for sampling strategy and “b” stands for the batch size. Applying Interest Region Sampling improves the accuracy by 15% across various batch sizes. Larger batch sizes can improve accuracy while reducing the number of gradient steps needed for convergence.

To remove the cluttered background in test images, we use the publicly available segmentation masks provided by DenseFusion [47]. Our pipeline consists of two stages: 1) feature-based pose initialization, and 2) iNeRF pose refinement.

Evaluation Metric. We evaluate our method with the ADD [9] and ADD-S [14] metrics. ADD measures the average distance between points after being transformed by the ground truth and predicted poses. ADD-S is used for

symmetric objects (*e.g.*, *Eggbox* and *Glue*) and instead measures the average distance to the closest point rather than the ground truth point. We report the percentage of poses that yield an ADD(-S) metric of less than 10% of the object’s diameter.

5.3.1 Feature-based Initialization.

We perform initial pose estimation with SfM by matching synthetic training images augmented with fixed rotations (90° , 180° , 270°) against masked test images. We find that

Train data	With Real Pose Labels		Without Real Pose Labels					
	Methods	DPOD[51]	DeepIM[14]	AAE[39]	MHP [20]	DPOD[51]	Self6D[48]	Ours-init
Ape	53.3	77	4.0	11.9	35.1	38.9	38.6	51.0
Bvise	95.2	97.5	20.9	66.2	59.4	75.2	96.6	95.8
Cam	90.0	93.5	30.5	22.4	15.5	36.9	91.9	90.6
Can	94.1	96.5	35.9	59.8	48.8	65.6	79.5	80.1
Cat	60.4	82.1	17.9	26.9	28.1	57.9	78.1	82.2
Drill	97.4	95.0	24.0	44.6	59.3	67.0	84.6	84.2
Duck	66.0	77.7	4.9	8.3	25.6	19.6	21.2	27.8
Eggbox	99.6	97.1	81.0	55.7	51.2	99.0	94.4	95.6
Glue	93.8	99.4	45.5	54.6	34.6	94.1	61.7	88.2
Holep	64.9	52.8	17.6	15.5	17.7	16.2	75.9	73.8
Iron	99.8	98.3	32.0	60.8	84.7	77.9	87.0	88.1
Lamp	88.1	97.5	60.5	-	45.0	68.2	86.4	85.8
Phone	71.4	87.7	33.8	34.4	20.9	50.1	87.1	86.8
Mean	82.6	88.6	31.4	38.8	40.5	58.9	75.6	79.2

Table 2: Quantitative results for the LineMOD dataset. We report performance using the Average Recall(%) of the ADD(-S) metric. “With Real Pose Labels” refers to methods that additionally train on 15% of the test data following [2] and therefore have seen real posed images, rather than only synthetic posed images.

rotation augmentation is crucial because feature descriptor is not rotation-equivariant. Specifically, we first apply SuperPoint [6] for feature extraction and SuperGlue [34] for correspondence matching. Then, a sparse 3D model of the object is reconstructed using triangulation. For each test image, its features are extracted and matched against all the training images to construct the 2D-3D correspondence. Then, we solve for the poses using the PnP-RANSAC [8] algorithm. We find that our initialization strategy based on learned local descriptors and matchers is more resilient to the sim-to-real gap, outperforming previous state-of-the-art solutions based on direct direction regression with render-and-compare refinement [48]. However, when the objects exhibit no distinctive texture or geometry structure (e.g., *Ape*, *Cat*, and *Duck*), our feature-based initialization fails.

5.3.2 iNeRF Refinement.

Loss. Since the sim-to-real domain gap is partially caused by lighting, we attempt to decouple its effect. Specifically, we transform both rendered and observed images from RGB to YUV space, and discard the light channel Y before computing the loss. See the supplement for details.

Results. We find that iNeRF complements our feature-based initialization, and is particularly helpful for objects without salient features. For *Ape*, *Cat*, *Duck*, and *Glue*, iNeRF achieves 12.4%, 4.1%, 6.6%, and 26.5% improvements respectively. However, we also notice that iNeRF’s reconstruction loss is not a good surrogate for alignment due to the sim-to-real domain gap and lighting variation. Therefore, applying iNeRF can slightly hurt the performance of

our initialization on certain objects. Overall, we observe a 3.6% improvement compared to the initialization.

6. Limitations and Future Work

Although iNeRF has shown promising results on pose estimation, there are three major limitations: (i) Despite lighting and occlusion can severely affect the performance of iNeRF, they are not modeled by our current formulation. One potential solution is to model appearance variation using transient latent codes as was done in NeRF-W [23] when training NeRFs, and jointly optimize these appearance codes alongside camera pose within iNeRF. Alternatively, training a NeRF to output robust visual features along with opacity and color may be a promising direction. (ii) The current iNeRF framework assumes a trained NeRF, which in turn requires known camera poses as supervision. In the real world, we don’t have a perfect strategy for camera calibration, so a promising future direction would be performing unsupervised learning by jointly optimizing a NeRF and the input images’ camera poses. (iii) Currently, iNeRF takes around 30 seconds to run 100 optimization steps, which prevents it from being practical for real-time use. We expect that this issue may be mitigated with recent improvements in NeRF’s rendering speed [17].

7. Conclusion

We have presented iNeRF, a framework for pose estimation that works by inverting a trained NeRF model. We have demonstrated that iNeRF is able to perform accurate pose estimation using gradient-based optimization. We have thoroughly investigated how to best construct mini-

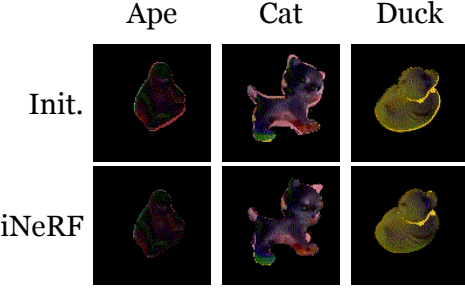


Figure 7: A visualization of the difference between rendered and observed images using the L1 norm. After iNeRF refinement, the area of the lighter region, which indicates higher error, is decreased. In all 3 examples, the refined poses result in ADD errors smaller than 10% diameter of the objects.

batches of sampled rays for iNeRF and have demonstrated its performance on both synthetic and real datasets. Lastly, we have shown how iNeRF can be used to improve NeRF reconstruction quality by allowing images without known pose labels to be used when training NeRF. This suggests a future research direction for jointly-optimized reconstruction and pose estimation.

Appendix

A. Qualitative Results on LineMOD

We show qualitative results before and after applying iNeRF in Figure 7. The differences between rendered and observed images are visualized, which show that iNeRF can update the initial estimated pose for better image alignment. This figure also shows some residual colors remain even when iNeRF estimates accurate pose. These residuals are due to a mismatch of color and lighting between the renderings of the synthetic model and the observed images.

B. Implementation Details

Adam Optimizer and Learning Rate Schedule. The hyperparameter β_1 is set to 0.9 and β_2 is set to 0.999 in Adam optimizer. We set the initial learning rate α_0 to 0.01. The learning rate at step t is set as follow:

$$\alpha_t = \alpha_0 0.8^{t/100}.$$

Loss for LineMOD. To compare the rendered and observed images, we transform both of them from RGB to YUV space using the standard definition:

$$\begin{bmatrix} Y \\ U \\ V \end{bmatrix} = \begin{bmatrix} 0.2126 & 0.7152 & 0.0722 \\ -0.09991 & -0.33609 & 0.436 \\ 0/615 & -0.55861 & -0.05639 \end{bmatrix} \begin{bmatrix} R \\ G \\ B \end{bmatrix}$$

The Y channel is not considered in the computation of loss.

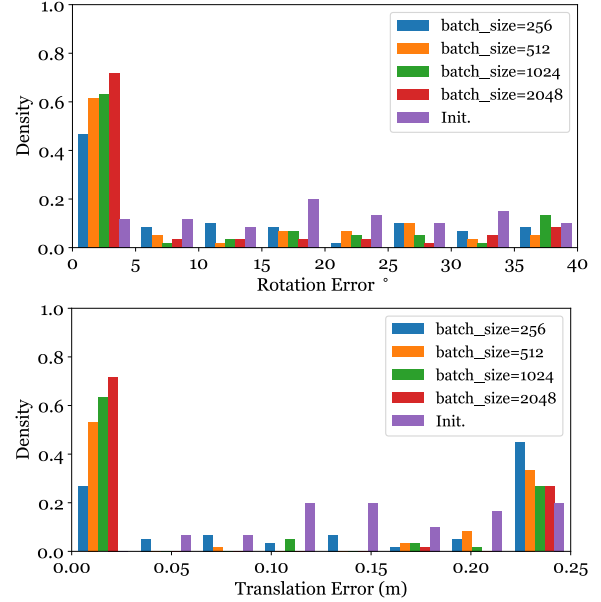


Figure 8: Histogram of pose errors on real-world scenes from the LLFF dataset.

C. Histogram of Pose Errors

We visualize the histogram of pose errors, before and after iNeRF optimization, on the LLFF dataset in Figure 8 using the data from Section 5.2. The data is generated by applying random perturbations within $[-40, 40]$ degrees for rotation and $[-0.1, 0.1]$ meters along each axis for translation. Note that when the batch size is 2048, more than 70% of the data has $< 5^\circ$ and < 5 cm error after iNeRF is applied.

D. Analysis: Per-Pixel Gradients

To help provide some introspection on the gradients optimized through the NeRF models, we may visualize the per-pixel partial derivatives of the photometric loss with respect to the 6 degrees of freedom for the pose during the optimization. Consider the loss separately for each pixel, with each pixel associated with some ray \mathbf{r} :

$$\mathcal{L}_{\text{per-pixel}} = \|\hat{C}(\mathbf{r}) - C(\mathbf{r})\|_2^2$$

To visualize the gradients spatially, consider the partial derivatives for this loss with respect to each of the six exponential coordinates:

$$\nabla_{S\theta} \mathcal{L}_{\text{per-pixel}} = \left[\frac{\partial \mathcal{L}_{\text{per-pixel}}}{\partial (S\theta)_1} \dots \frac{\partial \mathcal{L}_{\text{per-pixel}}}{\partial (S\theta)_6} \right]$$

If for each of these 6 partial derivatives, we plot the dense image of these values for each pixel, we obtain the image as shown in Fig. 9(a-f). The histogram of the distribution of the 6 partial derivatives is shown in Fig. 9(g-l). From these

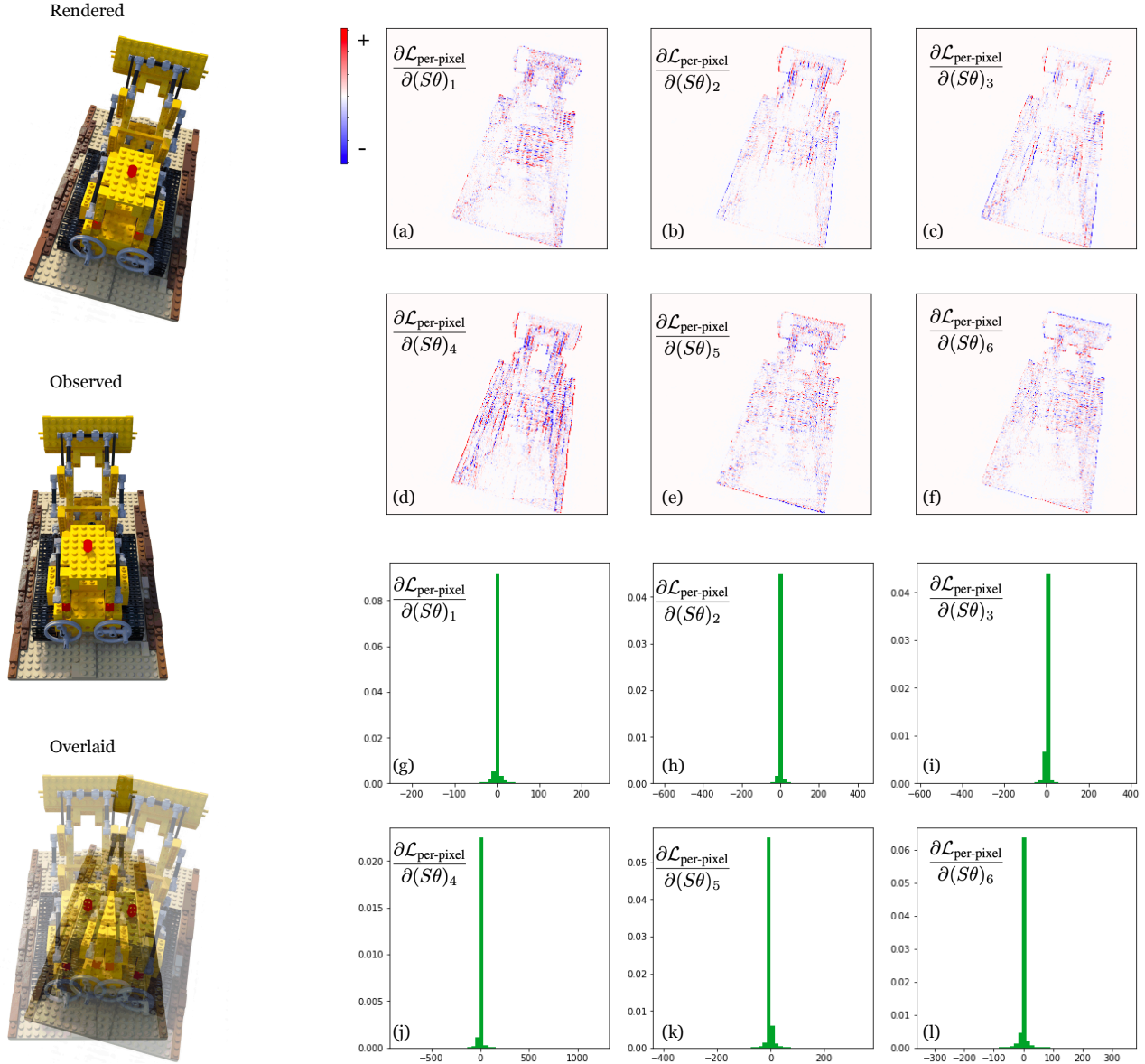


Figure 9: A depiction of the distribution of gradients optimized during iNeRF. On the left are shown the NeRF-rendered image for an initial pose estimate with 15 degree rotation error, the observed image, and the “overlaid” image, i.e. the alpha-blend of the above two. On the right, panels (a-f) depict, densely over the image for each pixel, the partial derivative $\frac{\partial \mathcal{L}_{\text{per-pixel}}}{\partial (S\theta)_i}$ for each of the six degrees of freedom, $i = \{1, 2, 3, 4, 5, 6\}$ of the exponential coordinates. Panels (g-l) show the histograms of the values of the partial derivatives.

plots, with the clean synthetic dataset, we learn that (i) the majority of gradients come from edges in the rendered image, (ii) the majority of the gradients are near zero in clean-background scenes, and (iii) the distribution of per-pixel partial derivatives with respect to each degree of freedom can be broad, with many pixels disagreeing on the direction of the gradient. Our results showing the practical convergence of iNeRF over reasonably wide initializations, for

example Fig. 8, suggest that the stochastic optimization is able to converge to useful optima despite these complicated distributions. The high proportion of zero-valued gradients also adds explanation for why our interest point sampling produces faster convergence.

E. More analysis in self-supervised NeRF

For the *Fern* scene, we found that when only 10% of labeled camera poses are used, it worsens the PSNR from 18.5 to 15.64. The results show that having enough labels for a good initialization is important.

References

- [1] Mathieu Aubry, Daniel Maturana, Alexei A Efros, Bryan C Russell, and Josef Sivic. Seeing 3D chairs: exemplar part-based 2D-3D alignment using a large dataset of CAD models. *CVPR*, 2014. [2](#)
- [2] Eric Brachmann, Frank Michel, Alexander Krull, Michael Ying Yang, Stefan Gumhold, et al. Uncertainty-driven 6d pose estimation of objects and scenes from a single rgb image. *CVPR*, 2016. [8](#)
- [3] Wenzheng Chen, Huan Ling, Jun Gao, Edward Smith, Jaakko Lehtinen, Alec Jacobson, and Sanja Fidler. Learning to predict 3d objects with an interpolation-based differentiable renderer. *NeurIPS*, 2019. [2](#)
- [4] Xu Chen, Zijian Dong, Jie Song, Andreas Geiger, and Otmar Hilliges. Category level object pose estimation via neural analysis-by-synthesis. *ECCV*, 2020. [2, 3](#)
- [5] Alvaro Collet, Manuel Martinez, and Siddhartha S Srinivasa. The moped framework: Object recognition and pose estimation for manipulation. *IJRR*, 2011. [2](#)
- [6] Daniel DeTone, Tomasz Malisiewicz, and Andrew Rabenovich. Superpoint: Self-supervised interest point detection and description. *CVPR Workshops*, 2018. [8](#)
- [7] Vittorio Ferrari, Tinne Tuytelaars, and Luc Van Gool. Simultaneous object recognition and segmentation from single or multiple model views. *IJCV*, 2006. [2](#)
- [8] Martin A Fischler and Robert C Bolles. Random sample consensus: a paradigm for model fitting with applications to image analysis and automated cartography. *Communications of the ACM*, 1981. [8](#)
- [9] Stefan Hinterstoisser, Vincent Lepetit, Slobodan Ilic, Stefan Holzer, Gary Bradski, Kurt Konolige, and Nassir Navab. Model based training, detection and pose estimation of texture-less 3d objects in heavily cluttered scenes. *ACCV*, 2012. [6, 7](#)
- [10] Tomas Hodan, Frank Michel, Eric Brachmann, Wadim Kehl, Anders GlentBuch, Dirk Kraft, Bertram Drost, Joel Vidal, Stephan Ihrke, Xenophon Zabulis, et al. Bop: Benchmark for 6d object pose estimation. *ECCV*, 2018. [6](#)
- [11] James T. Kajiya and Brian P. Von Herzen. Ray tracing volume densities. *SIGGRAPH*, 1984. [3](#)
- [12] Hiroharu Kato, Deniz Beker, Mihai Morariu, Takahiro Ando, Toru Matsuoka, Wadim Kehl, and Adrien Gaidon. Differentiable rendering: A survey. *arXiv preprint arXiv:2006.12057*, 2020. [2](#)
- [13] Diederik P Kingma and Jimmy Ba. Adam: A method for stochastic optimization. *ICLR*, 2015. [4](#)
- [14] Yi Li, Gu Wang, Xiangyang Ji, Yu Xiang, and Dieter Fox. Deepim: Deep iterative matching for 6d pose estimation. *ECCV*, 2018. [6, 7, 8](#)
- [15] Chen-Hsuan Lin, Chaoyang Wang, and Simon Lucey. Sdf-srn: Learning signed distance 3d object reconstruction from static images. *NeurIPS*, 2020. [2](#)
- [16] Chen-Hsuan Lin, Oliver Wang, Bryan C Russell, Eli Shechtman, Vladimir G Kim, Matthew Fisher, and Simon Lucey. Photometric mesh optimization for video-aligned 3d object reconstruction. In *Proceedings of the IEEE Conference on Computer Vision and Pattern Recognition*, pages 969–978, 2019. [2](#)
- [17] Lingjie Liu, Jiatao Gu, Kyaw Zaw Lin, Tat-Seng Chua, and Christian Theobalt. Neural sparse voxel fields. *NeurIPS*, 2020. [2, 8](#)
- [18] Kevin M Lynch and Frank C Park. *Modern Robotics*. Cambridge University Press, 2017. [4](#)
- [19] Wei-Chiu Ma, Shenlong Wang, Jiayuan Gu, Sivabalan Manivasagam, Antonio Torralba, and Raquel Urtasun. Deep feedback inverse problem solver. *ECCV*, 2020. [2](#)
- [20] Fabian Manhardt, Diego Martin Arroyo, Christian Rupprecht, Benjamin Busam, Tolga Birdal, Nassir Navab, and Federico Tombari. Explaining the ambiguity of object detection and 6d pose from visual data. *CVPR*, 2019. [8](#)
- [21] Lucas Manuelli, Wei Gao, Peter Florence, and Russ Tedrake. kPAM: Keypoint affordances for category-level robotic manipulation. *ISRR*, 2019. [1](#)
- [22] Pat Marion, Peter R Florence, Lucas Manuelli, and Russ Tedrake. Label fusion: A pipeline for generating ground truth labels for real rgbd data of cluttered scenes. *ICRA*, 2018. [1](#)
- [23] Ricardo Martin-Brualla, Noha Radwan, Mehdi SM Sajjadi, Jonathan T Barron, Alexey Dosovitskiy, and Daniel Duckworth. Nerf in the wild: Neural radiance fields for unconstrained photo collections. *arXiv preprint arXiv:2008.02268*, 2020. [2, 8](#)
- [24] Nelson Max. Optical models for direct volume rendering. *IEEE TVCG*, 1995. [3](#)
- [25] Lars Mescheder, Michael Oechsle, Michael Niemeyer, Sebastian Nowozin, and Andreas Geiger. Occupancy networks: Learning 3d reconstruction in function space. *CVPR*, 2019. [2](#)
- [26] Ben Mildenhall, Pratul P Srinivasan, Rodrigo Ortiz-Cayon, Nima Khademi Kalantari, Ravi Ramamoorthi, Ren Ng, and Abhishek Kar. Local light field fusion: Practical view synthesis with prescriptive sampling guidelines. *ACM TOG*, 2019. [5](#)
- [27] Ben Mildenhall, Pratul P Srinivasan, Matthew Tancik, Jonathan T Barron, Ravi Ramamoorthi, and Ren Ng. Nerf: Representing scenes as neural radiance fields for view synthesis. *arXiv preprint arXiv:2003.08934*, 2020. [2, 3, 5, 6](#)
- [28] Michael Niemeyer, Lars Mescheder, Michael Oechsle, and Andreas Geiger. Differentiable volumetric rendering: Learning implicit 3d representations without 3d supervision. *CVPR*, 2020. [2](#)
- [29] Andrea Palazzi, Luca Bergamini, Simone Calderara, and Rita Cucchiara. End-to-end 6-DOF object pose estimation through differentiable rasterization. *ECCV*, 2018. [2](#)
- [30] Jeong Joon Park, Peter Florence, Julian Straub, Richard Newcombe, and Steven Lovegrove. Deepsdf: Learning con-

tinuous signed distance functions for shape representation. *CVPR*, 2019. 2

[31] Keunhong Park, Arsalan Mousavian, Yu Xiang, and Dieter Fox. Latentfusion: End-to-end differentiable reconstruction and rendering for unseen object pose estimation. *CVPR*, 2020. 2

[32] Georgios Pavlakos, Xiaowei Zhou, Aaron Chan, Konstantinos G Derpanis, and Kostas Daniilidis. 6-DOF object pose from semantic keypoints. *ICRA*, 2017. 2

[33] Fred Rothganger, Svetlana Lazebnik, Cordelia Schmid, and Jean Ponce. 3d object modeling and recognition using local affine-invariant image descriptors and multi-view spatial constraints. *IJCV*, 2006. 2

[34] Paul-Edouard Sarlin, Daniel DeTone, Tomasz Malisiewicz, and Andrew Rabinovich. SuperGlue: Learning feature matching with graph neural networks. *CVPR*, 2020. 8

[35] Tanner Schmidt, Richard Newcombe, and Dieter Fox. Self-supervised visual descriptor learning for dense correspondence. *IEEE Robotics and Automation Letters*, 2016. 3

[36] Max Schwarz, Hannes Schulz, and Sven Behnke. Rgb-d object recognition and pose estimation based on pre-trained convolutional neural network features. *ICRA*, 2015. 2

[37] Jamie Shotton, Ben Glocker, Christopher Zach, Shahram Izadi, Antonio Criminisi, and Andrew Fitzgibbon. Scene coordinate regression forests for camera relocalization in rgb-d images. *CVPR*, 2013. 3

[38] Vincent Sitzmann, Michael Zollhöfer, and Gordon Wetzstein. Scene representation networks: Continuous 3d-structure-aware neural scene representations. *NeurIPS*, 2019. 2

[39] Martin Sundermeyer, Zoltan-Csaba Marton, Maximilian Durner, Manuel Brucker, and Rudolph Triebel. Implicit 3d orientation learning for 6d object detection from rgb images. *ECCV*, 2018. 8

[40] Supasorn Suwajanakorn, Noah Snavely, Jonathan J Tompson, and Mohammad Norouzi. Discovery of latent 3d keypoints via end-to-end geometric reasoning. *NeurIPS*, 2018. 2

[41] Richard Szeliski. Image alignment and stitching: A tutorial. *Foundations and Trends® in Computer Graphics and Vision*, 2006. 5

[42] Bugra Tekin, Sudipta N Sinha, and Pascal Fua. Real-time seamless single shot 6D object pose prediction. *CVPR*, 2018. 2

[43] Jonathan Tremblay, Thang To, Balakumar Sundaralingam, Yu Xiang, Dieter Fox, and Stan Birchfield. Deep object pose estimation for semantic robotic grasping of household objects. *CoRL*, 2018. 2

[44] Shubham Tulsiani and Jitendra Malik. Viewpoints and keypoints. *CVPR*, 2015. 2

[45] Julien Valentin, Matthias Nießner, Jamie Shotton, Andrew Fitzgibbon, Shahram Izadi, and Philip HS Torr. Exploiting uncertainty in regression forests for accurate camera relocalization. *CVPR*, 2015. 3

[46] Hans Wallach. Über visuell wahrgenommene bewegungsrichtung. *Psychologische Forschung*, 1935. 4

[47] Chen Wang, Danfei Xu, Yuke Zhu, Roberto Martín-Martín, Cewu Lu, Li Fei-Fei, and Silvio Savarese. Densefusion: 6d object pose estimation by iterative dense fusion. In *Proceedings of the IEEE Conference on Computer Vision and Pattern Recognition*, pages 3343–3352, 2019. 7

[48] Gu Wang, Fabian Manhardt, Jianzhun Shao, Xiangyang Ji, Nassir Navab, and Federico Tombari. Self6d: Self-supervised monocular 6d object pose estimation. *arXiv preprint arXiv:2004.06468*, 2020. 2, 4, 6, 8

[49] He Wang, Srinath Sridhar, Jingwei Huang, Julien Valentin, Shuran Song, and Leonidas J Guibas. Normalized object coordinate space for category-level 6d object pose and size estimation. *CVPR*, 2019. 3

[50] Yu Xiang, Tanner Schmidt, Venkatraman Narayanan, and Dieter Fox. PoseCNN: A convolutional neural network for 6D object pose estimation in cluttered scenes. *RSS*, 2018. 2

[51] Sergey Zakharov, Ivan Shugurov, and Slobodan Ilic. Dpod: 6d pose object detector and refiner. *ICCV*, 2019. 6, 8